

Article

Open Access



Scalable fabrication of inch-sized FAPbI_3 perovskite wafers for highly sensitive near-infrared photodetection

Chao Li[#], Zuolin Zhang[#], Chenglin Wang, Mengjia Li, Jike Ding, Cong Chen^{*}

State Key Laboratory of Reliability and Intelligence of Electrical Equipment, School of Materials Science and Engineering, Hebei University of Technology, Tianjin 300401, China.

[#]Authors contributed equally.

***Correspondence to:** Prof. Cong Chen, State Key Laboratory of Reliability and Intelligence of Electrical Equipment, School of Materials Science and Engineering, Hebei University of Technology, No. 5340, Xiping Road, Beichen District, Tianjin 300401, China. E-mail: chencong@hebut.edu.cn

How to cite this article: Li C, Zhang Z, Wang C, Li M, Ding J, Chen C. Scalable fabrication of inch-sized FAPbI_3 perovskite wafers for highly sensitive near-infrared photodetection. *Energy Mater* 2024;4:400077. <https://dx.doi.org/10.20517/energymater.2024.54>

Received: 30 May 2024 **First Decision:** 26 Jun 2024 **Revised:** 8 Jul 2024 **Accepted:** 13 Aug 2024 **Published:** 6 Sep 2024

Academic Editors: Soo Young Kim, Chunhui Duan, Weihua Tang **Copy Editor:** Fangling Lan **Production Editor:** Fangling Lan

Abstract

Perovskite wafers, with superior optoelectronic properties and stability, show great promise for photovoltaic and photoelectric applications. However, traditional solution growth methods struggle with crystallization control and phase purity, while solid-phase synthesis methods encounter high-density grain boundary traps. To tackle these issues, we devised a scalable method combining physical thermal field and chemical bonding to fabricate inch-sized FAPbI_3 wafers, enabling efficient near-infrared photodetection. By integrating a 120 °C hot-pressing to stabilize the photoactive α phase and polyaniline polymer to conduct and passivate the grain boundaries, we obtained quasi-single crystal FAPbI_3 wafers on a large scale. This approach overcomes the critical challenges of phase impurities and high-density defects, enhancing the phase stability of the FAPbI_3 wafers. As a result, the FAPbI_3 wafer-based photodetector exhibits an impressive external quantum efficiency of 312% at 854 nm near-infrared wavelength at 5 V bias, accompanied by a detectivity (D^*) of 4.69×10^{14} Jones and rapid response time in microsecond-scale. This performance surpasses conventional solution-grown single crystals, providing a scalable foundation for future integrated perovskite optoelectronic devices.

Keywords: FAPbI_3 wafer, NIR photodetectors, hot-pressing, conductive polyaniline polymers, grain boundary



© The Author(s) 2024. **Open Access** This article is licensed under a Creative Commons Attribution 4.0 International License (<https://creativecommons.org/licenses/by/4.0/>), which permits unrestricted use, sharing, adaptation, distribution and reproduction in any medium or format, for any purpose, even commercially, as long as you give appropriate credit to the original author(s) and the source, provide a link to the Creative Commons license, and indicate if changes were made.



INTRODUCTION

Near-infrared (NIR) photodetection technology holds significant importance in various domains, including medicine^[1], biological imaging^[2], and environmental monitoring^[3]. The conventional and commercial NIR photodetectors are predominantly formed from inorganic narrow-bandgap materials such as silicon (Si)^[4], germanium (Ge)^[5,6], indium gallium arsenide (InGaAs)^[7,8], lead selenide (PbSe)^[9,10], polymers^[11,12] and graphene^[13-16]. Recently, organic-inorganic hybrid perovskites have stood out in the field of NIR photodetectors due to their narrowed bandgap, high absorption coefficients, long diffusion lengths, and low exciton binding energies^[17-19]. The performance of perovskite-based NIR photodetectors critically depends on the composition and microstructural characteristics, including lattice distortions, crystal orientation, grain size, morphology, *etc.*^[20,21]. Despite over a decade of innovations, the solution processing method for fabricating perovskite polycrystalline films encounters two major inherent challenges. Firstly, solution processing methods grapple with phase impurities from residual solvents, inconsistent batch quality, and ecological concerns stemming from solvent cost and toxicity^[22]. Secondly, non-equilibrium crystallization in perovskite polycrystalline films often results in defects and lattice stress, compromised ion migration issues with uncontrolled crystal orientation, and grain size uniformity^[23].

Perovskite single crystal and quasi-single wafers preserve intrinsic crystal structure, ideal semiconductor bandgap, and excellent optoelectronic performance, exhibiting superior advantages in large-scale production and ideal model materials for optoelectronic characteristic optimization and photoelectric parameter simulation verification^[24-26]. At present, perovskite single crystal and quasi-single wafers prepared by techniques such as spatial confinement growth and reverse temperature growth have achieved tremendous success in the fields of photodetectors and photovoltaic applications. However, their low production yield, long crystal growth process, and refined external temperature conditions, substantially limit their utility in massive photodetectors^[27], not to mention in the field of large-scale application of solar cells^[28].

Solid-state powder mechanical pressing, as a novel method for producing perovskite wafers, has recently been proposed^[24]. In this process, the high-quality perovskite wafers are prepared by inducing deformation and densification of perovskite powder under high pressure within a limited spatial range. This method can overcome the limitations of high-density defect states in polycrystalline films and the difficulty in scaling single crystals. In 2017, Shrestha *et al.* pioneered the use of a hydraulic press to apply precise pressure to methyl ammonium lead iodide (MAPbI₃) perovskite microcrystals to fabricate dense wafers^[24]. However, the weak stability of MA⁺ cations has become the main exploration and innovation direction of “MA-Free” perovskite-based optoelectronic devices. Formamidinium lead iodide (FAPbI₃), with a narrow bandgap of 1.45 eV, is suitable for highly sensitive response in 700-900 nm spectrum NIR light^[29]. Previous studies indicate that solution-processed FAPbI₃ films could exhibit reliable signal output, along with low noise current, which are crucial performance metrics in NIR detection. Until now, there has been almost no research on NIR photodetectors based on FAPbI₃ quasi-single crystal wafers, mainly due to the serious $\alpha \rightarrow \delta$ Phase transition issues. That is to say, for the FAPbI₃ single crystal with the narrowest bandgap, there still exists stability in phase transition. The research focus of FAPbI₃ single crystal is to stabilize FAPbI₃ and minimize surface interface defects to the greatest extent possible.

To solve the above phase stability and trap defect-related issues, strategies of doping and additive molecules have been attempted previously on FAPbI₃ films or crystals for photoelectric applications. For example, Dimethylammonium (DMA⁺)^[30-32], dodecylammonium (DA⁺)^[33], N, N-dimethyl-1,3-propane diammonium (DMePDA²⁺), and 1,4-butane diammonium (BDA²⁺)^[34] were developed to effectively stabilize the crystal phase of FAPbI₃. However, as a dutable impurity ion, the introduction of large-sized organic cations will

reduce the bandgap of perovskite and produce layered low-dimensional structures to restrict charge transfer. On the other hand, introducing additive engineering, such as small molecules^[35,36] and polymers^[37,38], is a feasible way to achieve defect passivation and stabilize crystal structure. For example, Yang *et al.* introduced poly(styrene-co-acrylonitrile) polymer into perovskite precursor solutions for passivating grain boundary (GB) and surface defects of films^[39]. Polyvinyl amine and polyvinyl alcohol have been shown to passivate internal defects within perovskites^[40,41]. However, despite the passivation of surface dangling bonds and uncoordinated Pb^{2+} , non-doping insulating or weakly conductive polymers often limit the charge transfer characteristics between grains, which will restrain the carrier transport in the perovskite light absorption layer and harm the photoelectric performance of the devices. Developing new strategies to simultaneously stabilize the FAPbI_3 crystal phase and effectively passivate bulk and GB defects is of importance for achieving high-quality quasi-single crystal FAPbI_3 wafers and efficient optoelectronic devices.

In this work, to address the common issue of phase stability and trap defects in perovskite wafers, we proposed a new strategy of high-quality inch-sized FAPbI_3 wafer through the coordination of a physical thermal field of 120 °C hot-pressing and chemical bonding by conductive polyaniline (PANI) polymer for achieving highly sensitive NIR photodetection. This strategy is the first and a universal batch for large-area bulk phase single crystal preparation. PANI, which contains both amino groups and benzene rings, is an intrinsically conducting polymer that possesses tunable electrical conductivity, allowing for effective charge transport within the FAPbI_3 wafer-based photodetector with high photo-response speed and sensitivity. The physical hot-pressing can suppress phase transition and stabilize the FAPbI_3 crystalline phase, while the chemical bonding of PANI can passivate defects on GBs. The hydrogen bonding between PANI and iodine ions in FAPbI_3 could reduce iodine vacancies and inhibit ion migration. Finally, the high-conductivity PANI-modified FAPbI_3 wafer can achieve stable and high-speed photodetection for NIR light.

EXPERIMENTAL SECTION

Materials

The material 2-Methoxyethanol (2-ME, 99.8%) was obtained from Macklin. Lead iodide (PbI_2 , 99.99%) was purchased from Xi'an Polymer Light Technology Corp. Formamidinium iodide (FAI, 99.9%) was obtained from Greatcell Solar Materials. PANI (98%) was purchased from Energy Chemical. Precisely, PANI, with the molecular formula $\text{C}_6\text{H}_7\text{N}$ and a molecular weight of 93.13, has a melting point greater than 330 °C (lit.). It has a boiling point of 116 °C and a density of 1.36 g/mL at 25 °C. These properties indicate that PANI is highly stable at elevated temperatures and has a relatively high density at room temperature. All the reagents and chemicals were used without further purification.

Preparation of the FAPbI_3 microcrystals and wafer

First, 15 mmol FAI and PbI_2 (1:1 mol ratio) were dissolved in 15 mL of 2-ME with magnetic stirring at 50 °C for 12 h. The precursor solution was then filtered. The filtered solution was placed in an oil bath at 120 °C with slow magnetic stirring for 2 h. A large number of black crystals appeared in the solution, which was filtered again and washed sequentially with 2-ME and isopropanol (IPA). Finally, the solution was placed in a vacuum oven at 100 °C. The prepared FAPbI_3 microcrystals were thoroughly ground into powder. By heating at 120 °C for 10 min and pressing at 20 MPa in the customized mechanical tablet press equipment (Ziyang Instrument and Meter Sales Center in Xiqing District, Tianjin City), the FAPbI_3 polycrystalline wafers were obtained. The PANI was thoroughly ground and then sieved through a 1,000 mesh sieve. After that, 1 mg of sieved PANI and 1 g of FAPbI_3 were thoroughly ground together, and then the resulting mixture was subjected to a hot-pressing process under the same conditions to prepare FAPbI_3 perovskite wafers. NIR photodetectors utilize a planar metal-semiconductor-metal structure, with 80 nm Au deposited on the wafer in a vacuum chamber by a thermal evaporator, where the electrode gap is 300 μm , electrode length is 7.4 mm, and electrode width is 300 μm .

Measurements

X-ray diffraction (XRD) patterns of the films were characterized by Rigaku SmartLab using Cu K α target radiation ($\lambda = 1.5405 \text{ \AA}$) with a power of 4 kW at a scanning rate of $10^\circ \text{ min}^{-1}$. The cross-sectional view of the device and the surface morphology of the films were scanned by field-emission scanning electron microscopy (SEM, JEOL 7610F) with a voltage of 3 kV. The steady-state photoluminescence (SSPL) and time-resolved photoluminescence (TRPL) were measured by the fluorescence spectrometers (FLS1000). The absorption spectra were measured in the range of 300 to 900 nm by a Shimadzu UV-1800 spectrometer at a medium-speed scanning rate. Atomic force microscopy and Kelvin probe force microscopy (KPFM) were measured by Agilent 5500 scanning probe microscopy in tapping mode. ESCALAB 250Xi equipment was utilized for X-ray photoelectron spectroscopy (XPS) measurements. External quantum efficiency (EQE) was tested using a QE-IRIS of Enlitech. Fourier transform infrared (FTIR) spectra were recorded using a BURKER VERTEX 80V FTIR Spectrometer. The J - V characterizations were measured using a Keithley 2400 source meter.

RESULTS AND DISCUSSION

Here, to obtain the wafers, we first prepared micrometer-scaled FAPbI₃ single crystals with crystal sizes ranging from 1 to 10 μm [Supplementary Figure 1] as raw materials using the inverse temperature crystallization method to ensure the accurate precursor ratios required. FAPbI₃ and PANI all exhibited high melting points exceeding 300 $^\circ\text{C}$, higher than the annealing temperature used in our experiments (120 $^\circ\text{C}$) [Supplementary Table 1]. Then, we fabricated the control FAPbI₃ wafers using a mechanical pressing (20 MPa) method at room temperature ($\sim 25^\circ\text{C}$) from the FAPbI₃ microcrystals [Supplementary Figure 2]. However, only applying a stress field to the powder usually results in incomplete grain growth, with abundant pinholes and GBs between grains [Figure 1A]. To overcome this, we introduced a physical thermal field of 120 $^\circ\text{C}$ annealing in the mechanical pressing process for producing the second type wafer, called P-FAPbI₃ wafer. The additional annealing process can promote the refusion and growth of FAPbI₃ powder and generate large-sized regular crystal wafers [Figure 1B]. The larger grain size can be related to the growth of small-sized perovskite microcrystals through Oswald ripening under high temperature and high pressure, improving their crystallinity and reducing GB density. However, the P-FAPbI₃ wafer still falls into the polycrystalline category due to the presence of numerous GBs. Abundant vacancies at GBs serve as the principal channels for ion migration. We further introduced the conductive PANI as additives in the hot pressing process for producing the third type of wafer, called P&C-FAPbI₃ wafer [Figure 1C]. Specifically, PANI and FAPbI₃ microcrystal powder were pre-mixed and hot-milled to ensure thorough mixing and uniform distribution of the PANI within the FAPbI₃. It is seen that PANI could induce the grown grain size of the FAPbI₃ wafer, accompanied by disappeared GBs and a smoother surface. The cross-sectional SEM image of the FAPbI₃ wafer proves the high quality and uniformity of our proposed P&C-FAPbI₃ wafer.

The above indicates that we have innovatively introduced a physical thermal field and chemical bonding joint strategy based on traditional mechanical pressing to prepare perovskite wafers, and achieved inch-sized high-quality FAPbI₃ wafers. During this process, the physical thermal field can induce the growth of FAPbI₃ grains, minimizing GBs, while chemical bonding can fill GBs and improve wafer conductivity. The overall process diagram is shown in Figure 1D. We expect that the hot-pressing will help to stabilize the crystal phase of FAPbI₃, while PANI will passivate the uncoordinated bonds at GBs of the wafer with high crystal structure stability. We fabricated wafers with a diameter of 2 cm and a thickness of 1 mm [Figure 1E]. In addition, we also prepared wafers with a radius of 0.5 cm [Supplementary Figure 3], demonstrating the high adaptability of our method. As shown in Figure 1F, the conductivity of the P&C-

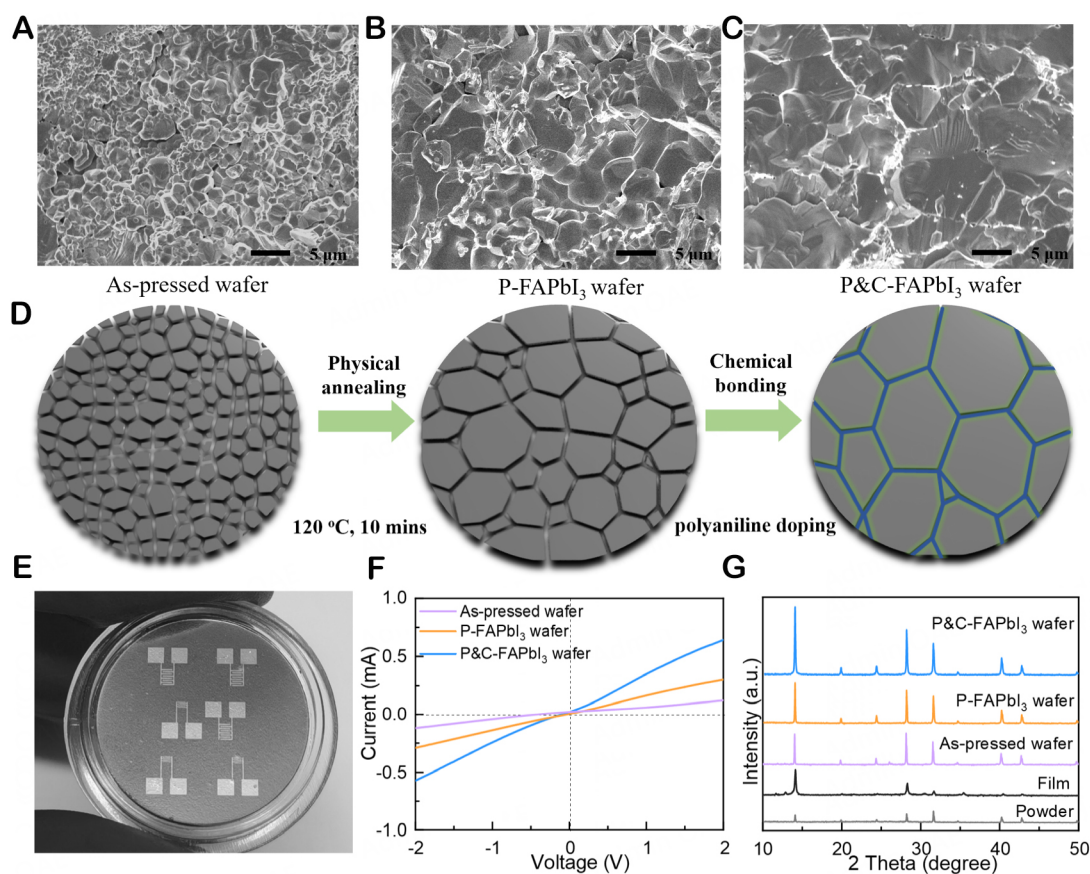


Figure 1. SEM of (A) as-pressed FAPbI₃ wafer, (B) P-FAPbI₃ wafer, and (C) P&C-FAPbI₃ wafer. (D) The schematic diagram from as-pressed FAPbI₃ wafer, to P-FAPbI₃ wafer, and then to P&C-FAPbI₃ wafer. (E) The photo of a planar structured photodetector based on the P&C-FAPbI₃ wafer. (F) I-V curves of the P&C-FAPbI₃ wafer-based photodetectors. (G) XRD patterns spectra of the powder, solution-processed FAPbI₃ film, as-pressed wafer, P-FAPbI₃ wafer, and P&C-FAPbI₃ wafer.

FAPbI₃ wafer exceeds 10^{-5} S/cm, which is higher than that of the as-pressed wafer, P-FAPbI₃ wafer and FAPbI₃ film counterpart [Supplementary Figure 4]^[42,43]. The enhanced conductivity can be attributed to the high conductivity of PANI and its effect on suppressing defects^[44,45]. Additionally, the higher conductivity is favored to reduce the noise current of the photodetector.

We then carried out XRD measurements on the three kinds of wafers [Figure 1G]. The typical solution-processed FAPbI₃ film by spin-coating and the as-synthesized FAPbI₃ powder was also introduced for comparison. The diffraction peaks of the FAPbI₃ wafers were in complete alignment with those of the powder. Solution-processed films exhibited characteristic XRD peaks at 11.7° and 12.6°^[46], corresponding to the non-ideal products δ -FAPbI₃ and PbI₂. However, we found that the wafers did not exhibit the characteristic peaks of PbI₂ impurity peaks or phase transition. Meanwhile, the intensity of typical XRD characteristic diffraction peaks such as [100] and [110] on P-FAPbI₃ wafers is much higher than that of directly synthesized FAPbI₃ microcrystal powders, demonstrating that using microcrystals as raw materials ensures phase purity and high crystalline quality of the wafers. More importantly, PANI will further enhance the intensity of characteristic diffraction peaks at 14.1° and 28.2°, indicating the superior crystal quality in the PANI-treated FAPbI₃ wafers. These results are attributed to the cross-linking of GBs by highly conductive PANI, effectively reducing GB distribution.

Additionally, the chemical interaction between amine groups and iodine by hydrogen bond could stabilize the iodine sites, reducing vacancies and inhibiting ion migration, as shown in [Figure 2A](#). To understand the chemical interaction mechanism between PANI and FAPbI₃, we carried out XPS and FTIR on both as-pressed FAPbI₃ wafers and P&C-FAPbI₃ wafer. Peaks corresponding to the C-N-C stretching vibration at 1,285.7 cm⁻¹ and the C-H stretching vibration at 871.6 cm⁻¹ were observed and shifted to 1,260.6 and 917.5 cm⁻¹ in the P&C-FAPbI₃ wafer, indicating that PANI was successfully incorporated [[Figure 2B](#)]. From the conducted XPS of I 3d [[Figure 2C](#)], we can observe that the binding energy peaks of I 3d shifted from 630.3 and 618.8 eV to 630.4 and 618.9 eV, respectively. Further, the binding energy peaks of Pb 4f [[Supplementary Figure 5](#)] shifted from 142.9 and 138.0 eV to 142.8 and 137.9 eV, respectively. The shift of the I characteristic peak further illustrates the hydrogen bonding between the amino group in the PANI molecule and I⁻ in FAPbI₃.

The ultraviolet-visible (UV-vis) absorption spectra of solution-processed FAPbI₃ films, as-pressed FAPbI₃ wafers, P-FAPbI₃ wafers, and P&C-FAPbI₃ wafers were compared in [Figure 2D](#). It is evident that the absorption intensity of three types of wafers increases sharply at the absorption edge and remains higher than that of the film samples across the 500-900 nm range. The enhanced absorption performance from film to wafers is attributed to the superior crystal quality of the wafers fabricated by the pressing method. After hot pressing and PANI modification in the P&C-FAPbI₃ wafer, the further improved absorption intensity is related to the enhanced crystal quality and reduced GBs. It is worth noticing that the absorption edges of the bare FAPbI₃ wafers and PANI-modified FAPbI₃ wafers could reach ~900 nm, surpassing that of the bare perovskite film. There is an obvious “cut-off” feature in the absorption spectrum, indicating that the FAPbI₃ wafer has a direct bandgap, in excellent agreement with previous research^[47]. This may be attributed to the result of crystallinity and an indirect bandgap transition, causing a reduction in the optical bandgap of the thicker wafers^[48]. From the Tauc plot shown in [Figure 2E](#), the results show that the optical bandgaps for the as-pressed FAPbI₃ wafers, P-FAPbI₃ wafers, and P&C-FAPbI₃ wafers are 1.373, 1.370 and 1.367 eV, which are lower than 1.524 eV of the solution-processed FAPbI₃ films, extremely closer to the bandgap of FAPbI₃ single crystals.

Subsequently, SSPL and TRPL measurements were applied to further explore the enhanced crystalline quality of wafers [[Figure 2F and G](#)]. After thermal field and PANI modification, there was an increase in the SSPL intensity and the enhanced average TRPL carrier lifetime from 1.34 to 3.62 μs [[Supplementary Table 2](#)]. To gain a deep understanding of the mechanism of decreased trap defects, we also conducted TRPL measurements on the FAPbI₃/PANI powder and FAPbI₃ powder in [Supplementary Figure 6](#). The overlapping lifetime results indicate that no significant charge transfer occurs between FAPbI₃ and PANI. So, the elongation of the TRPL lifetime in the wafers can be attributed to the passivation effect of PANI on the defects of FAPbI₃. By reducing non-radiative recombination pathways through defect passivation, PANI enhances the overall PL lifetime of the wafers. These indicate that PANI modification contributes to enhanced crystallinity and crystal quality, reduced GBs, and suppressed non-radiative recombination. Notably, the wafer without and with PANI modification samples exhibited strong anti-Stokes shifts, which could be due to lattice strain-induced Rashba splitting affecting the PL bandgap^[49,50].

Dark currents were conducted on the three kinds of wafers. It can be observed that the P&C-FAPbI₃ wafers exhibited the lowest dark current densities [[Figure 2H](#)], indicating the suppressed carrier recombination with PANI modification. These results demonstrate that the additional physical thermal field could produce perovskite crystals of high crystalline quality and that PANI modification effectively reduces GB distribution and passivates halide defects, thereby lowering dark currents. We calculated the trap density in both the

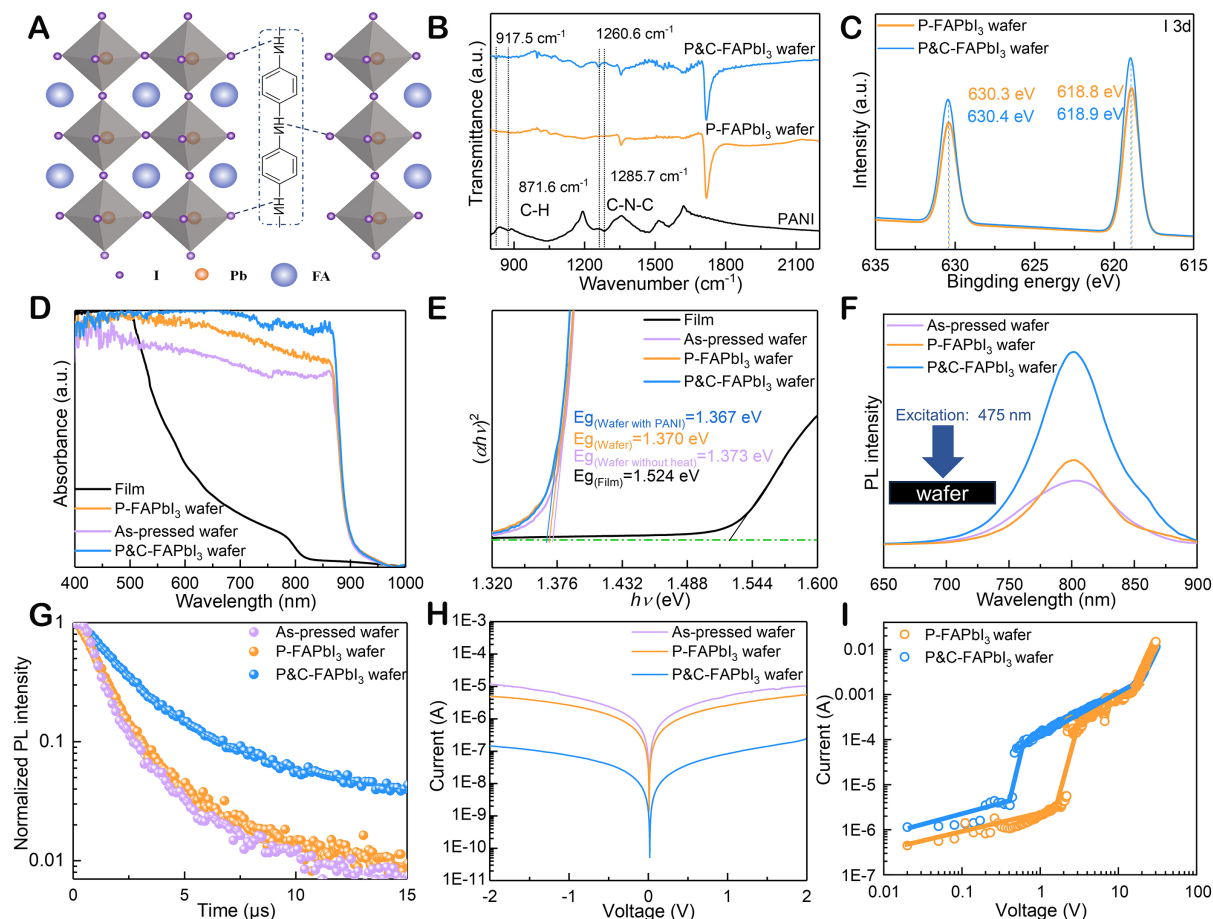


Figure 2. (A) The schematic illustration of the chemical interaction mechanism of PANI with the perovskite. (B) FTIR spectroscopy of PANI, as-pressed wafer, and P&C-FAPbI₃ wafer. (C) I 3d XPS spectra of the as-pressed wafer, and P&C-FAPbI₃ wafer. (D) UV-Vis absorption spectra of solution-processed film and wafers. (E) Tauc plot spectra of solution-processed perovskite film, as-pressed wafer, P-FAPbI₃ wafer, and the P&C-FAPbI₃ wafer. (F) SSPL and (G) TRPL spectra of the as-pressed wafer, P-FAPbI₃ wafer, and P&C-FAPbI₃ wafer with an excitation wavelength of 475 nm. (H) Dark I-V curves of the three wafers-based photodetectors. (I) Dark I-V curves of the hole transporting-only devices.

wafer and the wafer with PANI. Figure 2I shows the I-V curves of hole-only devices under dark conditions. Utilizing the theory of single-carrier space-charge-limited current (SCLC), the trap state density can be calculated from the trap filling limit voltage (V_{TFL}) derived from the measurement according to^[51]:

$$V_{TFL} = \frac{L^2 e N_t}{2 \epsilon \epsilon_0}$$

where ϵ and ϵ_0 represent the relative permittivity of the perovskite and vacuum permittivity, respectively [Supplementary Figure 7]. L is the thickness of the wafer (1 mm), e represents the elementary charge, and N_t indicates the density of the trap state. We calculated the trap density of the wafer to be $1.82 \times 10^{10} \text{ cm}^{-3}$ and that of the wafer with PANI modification to be $4.43 \times 10^9 \text{ cm}^{-3}$. Compared to previous studies, we found that the trap density in the wafer with PANI modification is lower than in polycrystalline films and close to single crystals^[52]. According to Mott-Gurney's law, a hole carrier mobility of $13.28 \text{ cm}^2 \text{ V}^{-1} \text{ s}^{-1}$ was derived at

a higher bias [Supplementary Figure 8]. This characteristic is attributed to the high-quality crystals and micron-scale particle size produced by the hot-pressing method.

To estimate the key photoresponse performance indicators for wafers [Figure 3A], we then conducted EQE measurements of the wafer-based photodetectors to reflect the ratio of photo-generated carriers to the number of incident photons. Photodetectors based on the P&C-FAPbI₃ wafers could exhibit the highest EQE of 312% at an NIR irradiation of 854 nm wavelength under a 5 V bias, which is higher than that of 215% and 272% for the as-pressed FAPbI₃ wafer and P-FAPbI₃ wafer-based devices [Figure 3B]. Within the 600–800 nm wavelength, the EQE spectrum shows a gradual increase. This behavior is typically associated with an increasing photoresponse due to the absorption of photons with energies higher than the bandgap, leading to the efficient generation of charge carriers. The rising trend indicates that the wafer is more efficient at converting incident photons into collected charges as the wavelength approaches the band edge. The drop in EQE between 800 and 820 nm could be attributed to several factors, such as interference effects within the device structure, non-radiative recombination processes, or the presence of defects and trap states that start to dominate the carrier dynamics. The sharp increase in EQE from 820 to 854 nm can be associated with the approach to the band edge of the wafer material, where the absorption coefficient typically increases sharply, leading to a higher photoresponse. The decrease in EQE beyond 854 nm is related to the lower photon energy for being insufficient to promote electrons across the bandgap, resulting in a diminished photoresponse. This decline marks the onset of the absorption edge, where the wafer material no longer absorbs photons efficiently, leading to a reduced EQE. In addition, the EQE value at 895 nm indicates that the wafer has good capacity of NIR extension^[53,54].

Responsivity (R) measures the output signal generated per unit of input optical power and is a key performance indicator for photodetectors. We calculated R values from the dark current and the EQE results. R can be expressed using^[18]:

$$R = \frac{I_{\text{light}} - I_{\text{dark}}}{P_0 S}$$

where I_{light} and I_{dark} are the light current and dark current, P_0 is the irradiance power density, and S is the effective illuminated area, 4.2 mm², where the distance between the electrodes is 100 μm. Photodetectors based on the annealed wafer with PANI modification exhibit the highest R value of 2.15 A/W at 854 nm wavelength, higher than that of 1.88 A/W for the annealed wafer and 1.49 A/W for the as-pressed wafer-based photodetectors [Supplementary Figure 9]. We further calculated the detectivity (D^*) of the photodetectors, which can be expressed by:

$$D^* = \frac{R}{\sqrt{2eI_d}}$$

where I_d represents the dark current. P&C-FAPbI₃ wafers-based photodetectors could exhibit a higher D^* -value of 4.69×10^{14} Jones at 854 nm wavelength, higher than that of 1.04×10^{14} Jones for P-FAPbI₃ wafers and 3.67×10^{13} Jones for the bare wafer [Figure 3C]. This suggests that PANI-modification has higher crystal quality and a lower density of defect states, facilitating photon absorption and charge generation while reducing non-radiative recombination.

Response speed is commonly used to evaluate a photodetection ability to track rapidly changing irradiation signals. Figure 3D–F shows the cyclic NIR response curves of the as-pressed wafer-based photodetector

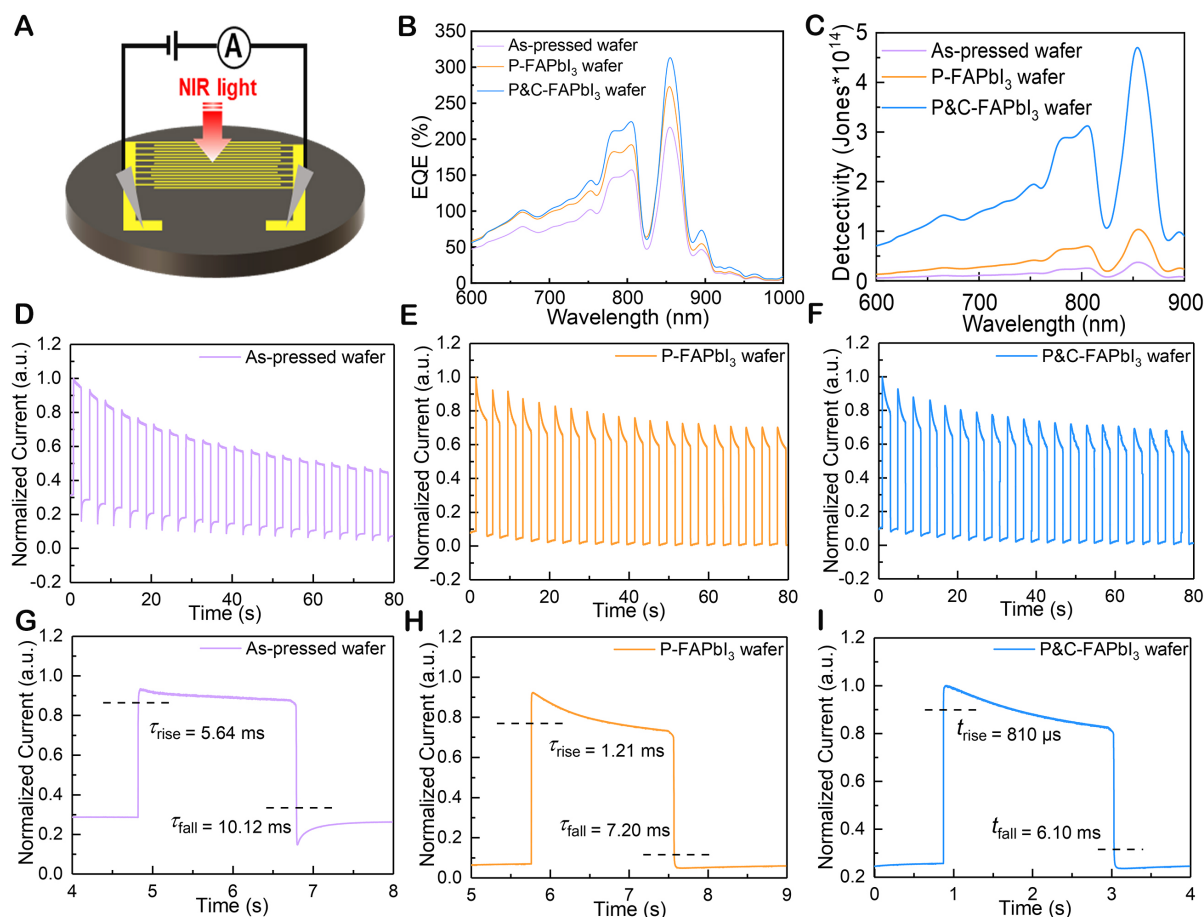


Figure 3. (A) The schematic diagram of the NIR response measurement. (B) EQE and (C) D^* of the photodetectors. The photocurrent response curves of photodetectors based on (D) the as-pressed wafer, (E) the P-FAPbI₃ wafer, and (F) the P&C-FAPbI₃ wafer under an 854 nm light source, respectively. The corresponding rise time from the enlarged photocurrent response curve of (D-F) wafers photodetectors is shown in the below part of (G-I).

[Figure 3D], the P-FAPbI₃ wafer [Figure 3E], and the P&C-FAPbI₃ wafer [Figure 3F] under a 5 V bias, tracking a periodically varying 854 nm NIR light source. Figure 3D shows the photocurrent response curve of the as-pressed wafer-based photodetector, lower than the photocurrent response curves of the P-FAPbI₃ wafer and P&C-FAPbI₃ wafer-based photodetectors. Further, there is an increase in current in the dark condition. These can be related to the more pinholes and boundaries at grain surface of the as-pressed wafer, increasing ion migration and resulting in severe carrier recombination in the dark state. Figure 3E and F shows higher response current and lower dark current, indicating that larger grains and fewer grain boundaries inhibit ion migration. Therefore, the carrier combination is suppressed. In the photocurrent response curves [Figure 3D-F], the photoelectric current of the as-pressed wafer detector is only 50% of its initial current after 80 s, while the P-FAPbI₃ wafer and the P&C-FAPbI₃ wafer-based photodetectors can maintain 80% of the initial photoelectric current. We also conducted photoresponse testing at a wavelength of 510 nm, exhibiting a continuous response with high repeatability [Supplementary Figure 10].

After multiple cyclic tests, the stability and current intensity performance of the P&C-FAPbI₃ wafer-based photodetectors is much more stable and higher than those of as-pressed wafer and the P-FAPbI₃ wafer-based photodetectors. The corresponding enlarged data was exhibited in Figure 3G-I, obtaining the rise

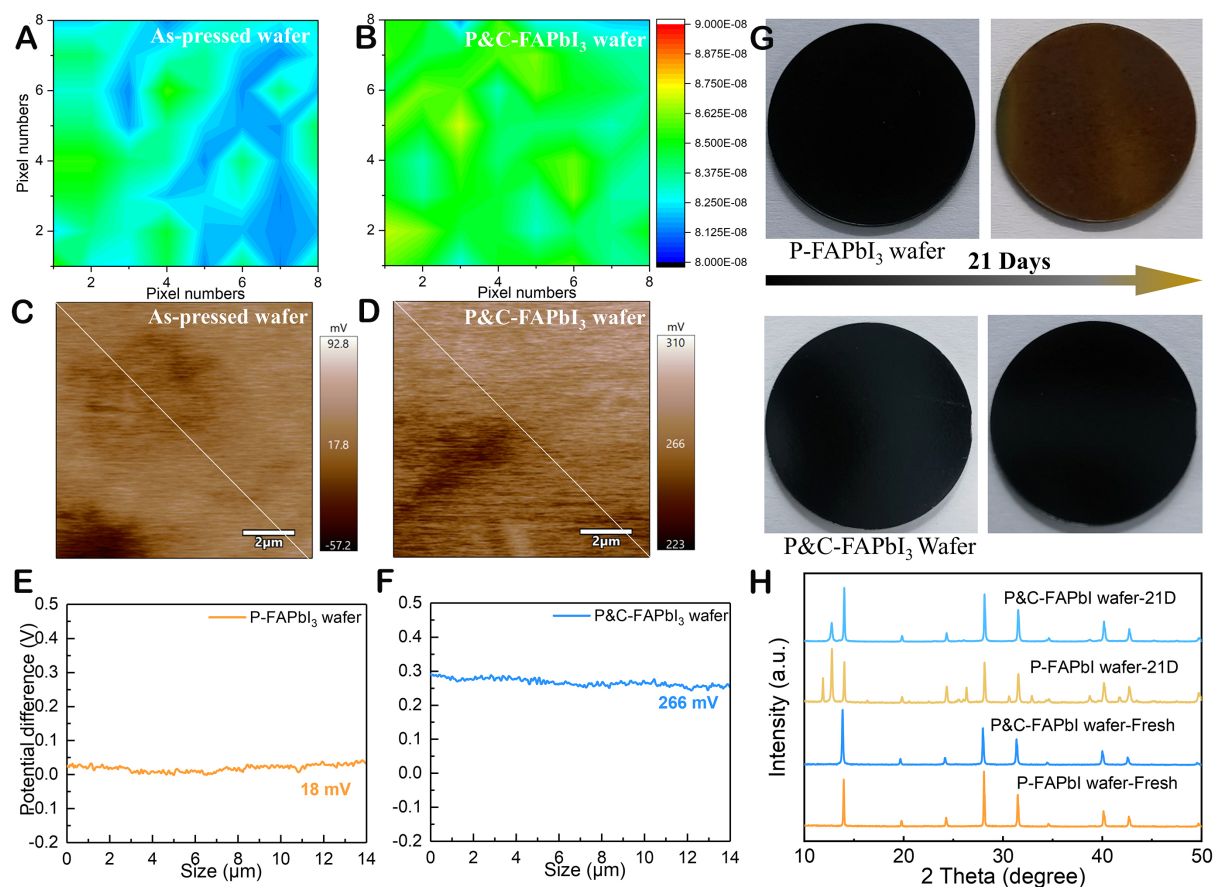


Figure 4. LBIC mapping of (A) the as-pressed wafer and (B) the P&C-FAPbI₃ wafer. KPFM images of (C) the as-pressed wafer and (D) the P&C-FAPbI₃ wafer. (E and F) The distribution of surface potential of the wafers from the KPFM. (G) Aged pictures and (H) XRD spectra of the as-pressed wafer and the P&C-FAPbI₃ wafer.

time (τ_{rise} , defined as the time taken to reach 90% of the steady state value) of the photodetector. The P&C-FAPbI₃ wafer-based photodetectors could exhibit the fastest response speeds of $\tau_{\text{rise}} = 703 \mu\text{s}$, faster than that of 1.21 ms for as-pressed wafer and 5.64 ms for the P&C-FAPbI₃ wafer. The achieved microsecond-level τ_{rise} response times are even quicker than some film or single-crystal photodetectors [Supplementary Table 3]. It is noteworthy that all the current cycle curve features a high current peak^[55]. Operational stability is also vital to the practical application of the photodetectors. Therefore, the stability characteristic of the P&C-FAPbI₃ wafer detector was determined. As exhibited in Supplementary Figure 11, the signal response of the P&C-FAPbI₃ wafer detector has almost no degradation during 100 s under ambient air conditions without encapsulation. Meanwhile, the photodetector not only yields a higher response current but also a lower dark current. These results demonstrate that PANI modification could exhibit enhanced spectral response capabilities and faster response times, which have significant implications for future NIR optical detection technologies.

To assess the intensity and uniformity of the photocurrent across the wafer surface, we employ light beam-induced current (LBIC) mapping for estimation. As shown in Figure 4A and B, compared with the as-pressed wafer, the P&C-FAPbI₃ wafer could achieve higher photocurrent and better uniformity, indicating that the physical hot pressing and chemical PANI modification could effectively suppress surface defects and ion migration. We also conduct the KPFM to measure the contact potential difference (CPD) to further

understand the mechanism behind the enhanced electrical performance [Figure 4C and D]. It can be calculated using $V_{CPD} = (\Phi_{tip} - \Phi_{sample})/e$. We then observed that P&C-FAPbI₃ wafers exhibit an overall higher surface potential distribution. Specifically, the average CPD value for the as-pressed wafer is 18 mV, while that for the P&C-FAPbI₃ wafer is 266 mV [Figure 4E]. The enhanced surface potential is related to the conductive PANI and favors the carrier injection efficiency.

The physical hot pressing and chemical bonding are beneficial for the phase stability of FAPbI₃ wafers, then we exposed the wafers to an air environment for 21 days at a temperature of 23 ± 3 °C and relative humidity (RH) of $50\% \pm 5\%$. The morphological changes of wafers in Figure 4F indicate the significant decomposition on the as-pressed wafer surface. In contrast, the P&C-FAPbI₃ wafer could retain the black phase for 21 days. XRD spectra of the as-pressed wafers revealed characteristic peaks at 11.7° and 12.6° , corresponding to δ -FAPbI₃ and PbI₂ of degradation products after aging [Figure 4G-H]. In contrast, the P&C-FAPbI₃ wafer showed only a partial appearance of PbI₂, indicating the high phase stability.

CONCLUSION

In summary, a rapid, scalable new strategy for the preparation of inch-sized FAPbI₃ perovskite wafers was developed. Specifically, based on traditional mechanical pressing, we further introduced a combination of physical thermal field (120 °C hot pressing) and chemical modification (PANI polymer bonding), achieving the crystal phase and defect stabilization of the pure FAPbI₃ crystal. The hydrogen bonding between PANI and FAPbI₃ can stabilize the [PbI₆]⁴⁻ octahedra. With the combination strategy, our photoconductive photodetector based on FAPbI₃ crystal can achieve a highly sensitive response to 854 nm NIR light, with an EQE of 312%, a D^* of 4.69×10^{14} Jones, and a fast microsecond-level response speed. This high response performance is comparable to that of single crystals prepared by traditional solution growth. We expect that this method will provide a scalable material basis for future wafer-scale perovskite optoelectronic integration technology.

DECLARATIONS

Authors' contributions

Conceived the ideas of the work and carried out the basic characterization, including XRD and XPS photovoltaic measurement: Wang C, Chen C

Prepared the perovskite wafers and the photodetector devices, and performed most measurements, including dark *I-V* curves and FTIR, EQE, cyclic stability, etc.: Li C, Wang C, Zhang Z

Helped to conduct the TRPL and PL measurements and analysis: Ding J, Li M

Involved in the data analysis and wrote the final version of the manuscript: Li C, Wang C, Chen C

Supervised this project: Chen C

All authors analyzed the data and contributed to the discussions.

Availability of data and materials

Some results of supporting the study are presented in the [Supplementary Materials](#). Other raw data that support the findings of this study are available from the corresponding author upon reasonable request.

Financial support and sponsorship

This work was supported by the National Natural Science Foundation of China (U21A2076), the S&T Program of Hebei (215676146H, 225676163GH), the Central Guidance on Local Science and Technology Development Fund of Hebei Province (226Z4305G), Hebei Province Higher Education Science and Technology Research Project (JZX2024030), Shijiazhuang Basic Research Project at Hebei-based Universities (241790847A), and the Natural Science Foundation of Hebei Province (E2024202086).

Conflicts of interest

All authors declared that there are no conflicts of interest.

Ethical approval and consent to participate

Not applicable.

Consent for publication

Not applicable.

Copyright

© The Author(s) 2024.

REFERENCES

1. Cai Y, Wei Z, Song C, Tang C, Han W, Dong X. Optical nano-agents in the second near-infrared window for biomedical applications. *Chem Soc Rev* 2019;48:22-37. DOI
2. Hong G, Antaris AL, Dai H. Near-infrared fluorophores for biomedical imaging. *Nat Biomed Eng* 2017;1:0010. DOI
3. Shang Z, Wu M, Meng Q, Jiao Y, Zhang Z, Zhang R. A near-infrared fluorescent probe for rapid and on-site detection of sulfur dioxide derivative in biological, food and environmental systems. *J Hazard Mater* 2024;465:133165. DOI
4. Kim W, Seo Y, Ahn D, et al. Monolithic perovskite-silicon dual-band photodetector for efficient spectral light discrimination. *Adv Sci* 2024;11:2308840. DOI PubMed PMC
5. Adinolfi V, Sargent EH. Photovoltage field-effect transistors. *Nature* 2017;542:324-7. DOI
6. Song L, Tang L, Hao Q, et al. Broadband photodetector based on SnTe nanofilm/n-Ge heterostructure. *Nanotechnology* 2022;33:425203. DOI
7. Wu D, Guo J, Wang C, et al. Ultrabroadband and high-detectivity photodetector based on WS₂/Ge heterojunction through defect engineering and interface passivation. *ACS Nano* 2021;15:10119-29. DOI
8. Mei L, Huang R, Shen C, et al. Hybrid halide perovskite-based near-infrared photodetectors and imaging arrays. *Adv Opt Mater* 2022;10:2102656. DOI
9. Ren YX, Dai TJ, He B, Liu XZ. Improvement on performances of graphene-PbSe Schottky photodetector via oxygen-sensitization of PbSe. *Mater Lett* 2019;236:194-6. DOI
10. Duan L, Hu L, Guan X, et al. Quantum dots for photovoltaics: a tale of two materials. *Adv Energy Mater* 2021;11:2100354. DOI
11. Gao Y, Zhao C, Pu K, et al. Low-voltage-modulated perovskite/organic dual-band photodetectors for visible and near-infrared imaging. *Sci Bull* 2022;67:1982-90. DOI
12. Li C, Wang H, Wang F, et al. Ultrafast and broadband photodetectors based on a perovskite/organic bulk heterojunction for large-dynamic-range imaging. *Light Sci Appl* 2020;9:31. DOI PubMed PMC
13. Liu CH, Chang YC, Norris TB, Zhong Z. Graphene photodetectors with ultra-broadband and high responsivity at room temperature. *Nat Nanotechnol* 2014;9:273-8. DOI PubMed
14. Arnold MS, Zimmerman JD, Renshaw CK, et al. Broad spectral response using carbon nanotube/organic semiconductor/C60 photodetectors. *Nano Lett* 2009;9:3354-8. DOI
15. Xie C, Nie B, Zeng L, et al. Core-shell heterojunction of silicon nanowire arrays and carbon quantum dots for photovoltaic devices and self-driven photodetectors. *ACS Nano* 2014;8:4015-22. DOI
16. Zhai T, Li L, Ma Y, et al. One-dimensional inorganic nanostructures: synthesis, field-emission and photodetection. *Chem Soc Rev* 2011;40:2986-3004. DOI
17. Rong Y, Hou X, Hu Y, et al. Synergy of ammonium chloride and moisture on perovskite crystallization for efficient printable mesoscopic solar cells. *Nat Commun* 2017;8:14555. DOI PubMed PMC
18. Zhou H, Zeng J, Song Z, et al. Self-powered all-inorganic perovskite microcrystal photodetectors with high detectivity. *J Phys Chem Lett* 2018;9:2043-8. DOI
19. Han Q, Bae SH, Sun P, et al. Single crystal formamidinium lead iodide (FAPbI₃): insight into the structural, optical, and electrical properties. *Adv Mater* 2016;28:2253-8. DOI
20. Wang H, Kim DH. Perovskite-based photodetectors: materials and devices. *Chem Soc Rev* 2017;46:5204-36. DOI PubMed
21. Muscarella LA, Hutter EM, Sanchez S, et al. Crystal orientation and grain size: do they determine optoelectronic properties of MAPbI₃ perovskite? *J Phys Chem Lett* 2019;10:6010-8. DOI
22. Elumalai N, Mahmud M, Wang D, Uddin A. Perovskite solar cells: progress and advancements. *Energies* 2016;9:861. DOI
23. Saki Z, Byranvand MM, Taghavinia N, Kedia M, Saliba M. Solution-processed perovskite thin-films: the journey from lab- to large-scale solar cells. *Energy Environ Sci* 2021;14:5690-722. DOI
24. Shrestha S, Fischer R, Matt GJ, et al. High-performance direct conversion X-ray detectors based on sintered hybrid lead triiodide perovskite wafers. *Nature Photon* 2017;11:436-40. DOI

25. Yang B, Pan W, Wu H, et al. Heteroepitaxial passivation of Cs₂AgBiBr₆ wafers with suppressed ionic migration for X-ray imaging. *Nat Commun* 2019;10:1989. DOI PubMed PMC
26. Jing H, Peng R, Ma RM, et al. Flexible ultrathin single-crystalline perovskite photodetector. *Nano Lett* 2020;20:7144-51. DOI
27. Leupold N, Panzer F. Recent advances and perspectives on powder-based halide perovskite film processing. *Adv Funct Mater* 2021;31:2007350. DOI
28. He Y, Matei L, Jung HJ, et al. High spectral resolution of gamma-rays at room temperature by perovskite CsPbBr₃ single crystals. *Nat Commun* 2018;9:1609. DOI PubMed PMC
29. Zheng Z, Wang S, Hu Y, Rong Y, Mei A, Han H. Development of formamidinium lead iodide-based perovskite solar cells: efficiency and stability. *Chem Sci* 2022;13:2167-83. DOI PubMed PMC
30. Ma C, Eickemeyer FT, Lee SH, et al. Unveiling facet-dependent degradation and facet engineering for stable perovskite solar cells. *Science* 2023;379:173-8. DOI
31. Lee JW, Tan S, Seok SI, Yang Y, Park NG. Rethinking the A cation in halide perovskites. *Science* 2022;375:eabj1186. DOI PubMed
32. Zhang Z, Li M, Li R, et al. Suppressing ion migration by synergistic engineering of anion and cation toward high-performance inverted perovskite solar cells and modules. *Adv Mater* 2024;36:e2313860. DOI
33. Tan S, Huang T, Yavuz I, et al. Stability-limiting heterointerfaces of perovskite photovoltaics. *Nature* 2022;605:268-73. DOI
34. Zhang F, Park SY, Yao C, et al. Metastable Dion-Jacobson 2D structure enables efficient and stable perovskite solar cells. *Science* 2022;375:71-6. DOI
35. Li C, Wang X, Bi E, et al. Rational design of Lewis base molecules for stable and efficient inverted perovskite solar cells. *Science* 2023;379:690-4. DOI
36. Zhao C, Zhang Q, Lyu Y, et al. Design of bridge molecules for high-efficiency FAPbI₃-based perovskite solar cells. *ACS Energy Lett* 2024;9:1405-14. DOI
37. Li M, Sun R, Chang J, et al. Orientated crystallization of FA-based perovskite via hydrogen-bonded polymer network for efficient and stable solar cells. *Nat Commun* 2023;14:573. DOI PubMed PMC
38. Zhao C, Zhang H, Almalki M, et al. Stabilization of FAPbI₃ with multifunctional alkali-functionalized polymer. *Adv Mater* 2023;35:e2211619. DOI
39. Yang J, Cao Q, He Z, et al. The poly(styrene-co-acrylonitrile) polymer assisted preparation of high-performance inverted perovskite solar cells with efficiency exceeding 22%. *Nano Energy* 2021;82:105731. DOI
40. Li H, Liang C, Liu Y, et al. Covalently connecting crystal grains with polyvinylammonium carboxyl chain backbone to suppress grain boundaries for long-term stable perovskite solar cells. *ACS Appl Mater Interfaces* 2017;9:6064-71. DOI
41. Sun Y, Wu Y, Fang X, et al. Long-term stability of organic-inorganic hybrid perovskite solar cells with high efficiency under high humidity conditions. *J Mater Chem A* 2017;5:1374-9. DOI
42. Liu X, Cui Q, Li H, et al. Biocompatible metal-free perovskite membranes for wearable X-ray detectors. *ACS Appl Mater Interfaces* 2024;16:16300-8. DOI
43. Baker CO, Huang X, Nelson W, Kaner RB. Polyaniline nanofibers: broadening applications for conducting polymers. *Chem Soc Rev* 2017;46:1510-25. DOI PubMed
44. Yang S, Dai J, Yu Z, et al. Tailoring passivation molecular structures for extremely small open-circuit voltage loss in perovskite solar cells. *J Am Chem Soc* 2019;141:5781-7. DOI
45. Wei D, Ma F, Wang R, et al. Ion-Migration inhibition by the cation- π interaction in perovskite materials for efficient and stable perovskite solar cells. *Adv Mater* 2018;30:e1707583. DOI
46. Liu F, Dong Q, Wong MK, et al. Is excess PbI₂ beneficial for perovskite solar cell performance? *Adv Energy Mater* 2016;6:1502206. DOI
47. Liu Y, Sun J, Yang Z, et al. 20-mm-large single-crystalline formamidinium-perovskite wafer for mass production of integrated photodetectors. *Adv Opt Mater* 2016;4:1829-37. DOI
48. Wang T, Daiber B, Frost JM, et al. Indirect to direct bandgap transition in methylammonium lead halide perovskite. *Energy Environ Sci* 2017;10:509-15. DOI
49. Zhou L, Neukirch AJ, Vogel DJ, et al. Density of states broadening in CH₃NH₃PbI₃ hybrid perovskites understood from ab initio molecular dynamics simulations. *ACS Energy Lett* 2018;3:787-93. DOI
50. Frohna K, Deshpande T, Harter J, et al. Inversion symmetry and bulk Rashba effect in methylammonium lead iodide perovskite single crystals. *Nat Commun* 2018;9:1829. DOI PubMed PMC
51. Gao D, Li R, Chen X, et al. Managing interfacial defects and carriers by synergistic modulation of functional groups and spatial conformation for high-performance perovskite photovoltaics based on vacuum flash method. *Adv Mater* 2023;35:e2301028. DOI
52. Zheng L, Nozariasbmarz A, Hou Y, et al. A universal all-solid synthesis for high throughput production of halide perovskite. *Nat Commun* 2022;13:7399. DOI PubMed PMC
53. Zhao D, Huang J, Qin R, Yang G, Yu J. Efficient visible-near-infrared hybrid Perovskite:PbS quantum dot photodetectors fabricated using an antisolvent additive solution process. *Adv Opt Mater* 2018;6:1800979. DOI
54. Li C, Lu J, Zhao Y, et al. Highly sensitive, fast response perovskite photodetectors demonstrated in weak light detection circuit and visible light communication system. *Small* 2019;15:e1903599. DOI
55. Ahmad V, Sobus J, Greenberg M, et al. Charge and exciton dynamics of OLEDs under high voltage nanosecond pulse: towards injection lasing. *Nat Commun* 2020;11:4310. DOI PubMed PMC